AD-A108 173 FOREIGN TECHNOLOGY DIV WRIGHT-PATTERSON AFB OH F/G 20/5
LASER JOURNAL (SELECTED ARTICLES),(U)
NOV 81 Z CHENGEN, S CHENG, Y CAILAI
UNCLASSIFIED FTD-ID(RS)T-0861-81 NL

END
DATE FILMED
82
DTIC

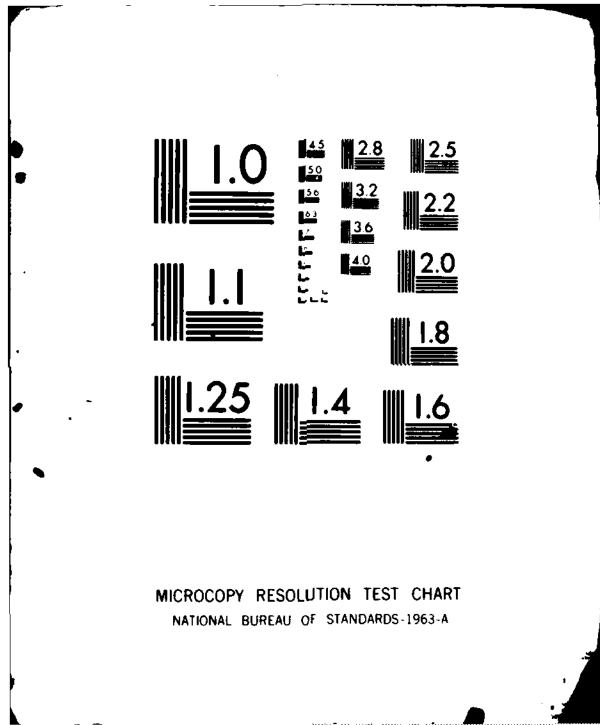
1.0
1.1
1.25
1.4
1.6
1.8
2.0
2.2
2.5
2.8
3.2
3.6
4.0
MICROCOPY RESOLUTION TEST CHART
NATIONAL BUREAU OF STANDARDS-1963-A

FTD-ID(RS)T-0861-81

AD A108173

FOREIGN TECHNOLOGY DIVISION

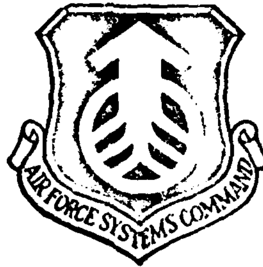

LASER JOURNAL
(Selected Articles)

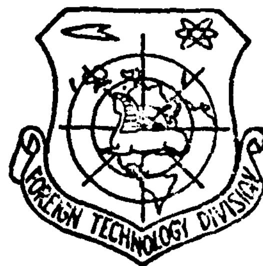

DTIC FILE COPY

1981

A

Approved for public release;
distribution unlimited.

81 12 08 143

EDITED TRANSLATION

FTD-ID(RS)T-0861-81 6 November 1981

MICROFICHE NR: FTD-81-C-001014

LASER JOURNAL (Selected Articles)

English pages: 27

Source: Laser Journal, Vol. 8, Nr. 2, 1981, pp. 5-9, 17-20, 47-49, 56-57

Country of origin: China
Translated by: SCITRAN
F33657-81-D-0263
Requester: FTD/TQTD
Approved for public release;distribution unlimited.

Accession For
NTIS GRA&I
DTIC TAB
Unannounced
Justification

A

THIS TRANSLATION IS A RENDITION OF THE ORIGINAL FOREIGN TEXT WITHOUT ANY ANALYTICAL OR EDITORIAL COMMENT. STATEMENTS OR THEORIES ADVOCATED OR IMPLIED ARE THOSE OF THE SOURCE AND DO NOT NECESSARILY REFLECT THE POSITION OR OPINION OF THE FOREIGN TECHNOLOGY DIVISION.

PREPARED BY:

TRANSLATION DIVISION
FOREIGN TECHNOLOGY DIVISION
WP-AFB, OHIO.

TABLE OF CONTENTS

Properties of Steady Discharge in Ar-Kr-F_2 Gas Mixture, by Zheng Chengen.................................. 1

UV-Preionized ArF and KrF Excimer Lasers, by Shangguan Cheng, Yuan Cailai, Ye Chao Dou Airong......... 12

ND:YAG Pulsed Laser Output at 1.064, 1.073, 1.061 and 1.052 μm Singlet Spectral Lines........................... 20

A New Feedback Controlled Current Stabilized Power Supply for Gas Laser, by Xie Guoliang, Shu Pujii, He Guopu.. 25

PROPERTIES OF STEADY DISCHARGE IN $Ar-Kr-F_2$ GAS MIXTURE*

Zheng Chengen

(Shanghai Institute of Optics and Fine Mechanics
Academia Sinica)

ABSTRACT

In this paper some properties of $Ar-Kr-F_2$ laser gas mixture plasma under steady discharge conditions are computed and discussed.

Inert gas halogen lasers attract people's attention because of their short wavelength, high efficiency, repeatable pulsed operation, high output power potential and wide energy band frequency tuning. Research indicates [1-3] that a pseudo-steady state operational process may exist in electron beam sustained discharge apparatus and X-ray pre-ionized discharge apparatus. In this process, such questions as what regulates the excitation rate of the discharging electrons and the distribution of the discharge energy, what effects do fluorine gas content and impurity gas (such as O_2) content have on the discharge property, etc., are all very important. Clarification of these questions will help us to further understand the properties of the discharge process of this type of plasma. In this paper we take the $Ar-Kr-F_2$ laser discharge gas as an example and discuss some computer simulations.

1. Computational method

In this paper, we limit our discussion to the range of pressures $E/P>2500$ volt/cm-at, ionization ratio $n_e/N<10^{-8}$ and metastable species ratio $N^*/N<10^{-8}$. Hence, in solving the Boltzmann integro-differential equations, we may neglect the e-e interaction term [1-4] and

*received December 21, 1979

the superelastic collision term between the electrons and the excited species. This condition corresponds to quite a sizable portion of pseudo-stable discharge processes in practical situations.

According to these simplifications, we may write the Boltzmann equation as

$$-\frac{dJ_f}{du}-\frac{dJ_{el}}{du}+\sum_{\alpha}(u+u_\alpha)f(u+u_\alpha)N_\alpha Q_\alpha(u+u_\alpha)-uf(u)N_\alpha Q_\alpha(u)=0 \tag{1}$$

where

$$J_f=\frac{-E^2}{3}\frac{u}{\sum_i N_i Q_m^i(u)}\cdot\frac{\partial f}{\partial u},$$

$$J_{el}'=-u^2\left(\sum_i \frac{2m}{M_i}N_i Q_m^i\right)\left(f+\frac{KT}{e}\frac{\partial f}{\partial u}\right),$$

The electron energy distribution function f satisfies the normalization condition

$$\int_0^\infty f\sqrt{u}\,du=1, \tag{2}$$

where u is the electron kinetic energy

$$u=\frac{\frac{1}{2}mV^2}{e};$$

m the electron mass; E the discharge field strength; M_i and N_i are respectively the mass and number density of the ith gas molecule (or atom; Q_m^i is the momentum transfer cross-section between the collision of the electron and the gas species; Q_α is the reaction cross-section between electron and the reaction type α; u_α is the energy loss of the electron in this process; N_α is the number density of the reaction type α.

The first term in Equation (1) is the effect of external electric field and the momentum transfer process on the energy space electron flow. The second term is the elastic collision effect of the momentum transfer process on the electron flow. The summation term is the inelastic collision effect between the electron and the particle. It includes the excitation and ionization of the particle by the electron, electron adhesion and other processes.

The electron energy distribution function $f(u)$, found from Equation (1) may be used to obtain the values of the following physical quantities:

Average electron energy

$$\bar{\varepsilon} = e\bar{u} = e\int_0^\infty du\, u^{3/2} f(u), \qquad (3)$$

The rate constant of the collision excitation or ionization of the neutral particle by the electron

$$R_\alpha = \sqrt{\frac{2e}{m}}\int_0^\infty du\, u f(u) Q_\alpha(u), \qquad (4)$$

The drift velocity of electron in the external field E

$$V_d = \frac{-1}{8}\sqrt{\frac{2e}{m}}\, E\int_0^\infty du\, u \times (\partial f/\partial u)/\sum_i N_i Q_m^i(u), \qquad (5)$$

Discharge power per unit volume

$$P = n_e W_e = e n_e V_d E, \qquad (6)$$

The fraction of discharge energy of the α process in the electron particle collision process

$$\eta_\alpha = u_\alpha N_\alpha \sqrt{\frac{2e}{m}}\int_0^\infty Q_\alpha u f\, du / E V_d, \qquad (7)$$

The fraction of discharge energy dissipated in the electron adhesion process

$$\eta_a = N_a \sqrt{\frac{2e}{m}} \int_0^\infty Q_a u^2 f \, du / EV_d, \quad (8)$$

The fraction of total discharge energy of electron-neutral particle momentum transfer process

$$\eta_m = \sum_i 2\sqrt{2me} \, \frac{N_i}{M_i} \int_0^\infty Q_m^i u^3 f \, du / EV_d. \quad (9)$$

In the summation term of Equation (1), we consider essentially the following reaction processes: momentum transfer processes between electron and Ar, Kr [6]; the dissociative-adhesion process between electron and F_2 [7]; the vibrational excitation process of electrons on F_2 [7]; sub-steady state collision excitation and ionization processes of electrons on Ar and Kr; the P state excitation process of electron on Ar and Kr [8-11]; collision excitation and ionization process [12-13] of electron on the P state atoms of Ar* and Kr*; collision ionization process [12] of electron on P state atoms.

In Equation (1), make the substitution

$$f(u)\sqrt{u}\,\Delta u \rightarrow n(u),$$

where $n(u)$ is the probability that the electron is between $u \rightarrow u+\Delta u$. Convert the equation to a difference scheme according to the Rockwood method. We limit our consideration of the electron energy range to 0∿20 electron volts and divide this energy axis evenly into 400 grids. The steady state solution is used [10]. The total computation is accomplished on a TQ-16 computer.

2. Electron energy distribution and electron excitation rate

The variation of the probability $n(\varepsilon)$ of the electron in the energy range $\varepsilon \rightarrow \varepsilon+\Delta\varepsilon$ with the electron energy is given in

Figure 1. The condition for the calculation is

$$Ar:Kr:F_2 = 0.915:0.08:0.005,$$

total pressure $P=2$ atmospheres, meta-stable species fractional density $N^*/N = 5\times10^{-4}$, , P state density $N^*(P) = 0.1N^*$, $\varepsilon = \varepsilon/u_0$ in the diagram. The computation indicates that within ∿10 electron volts, at $E/P = (2500-6000)$ volt/cm·atm, the electron energy distribution is not much affected by the variation in E/P. Figure 2 gives the variational relationship between the calculated average electron energy $\bar{\varepsilon}$ and E/P. It is clear that the average electron energy is generally about 5 electron volts. This value is about one order of magnitude higher than the average value of the electron energy of the electron-beam-controlled CO_2 laser plasma.

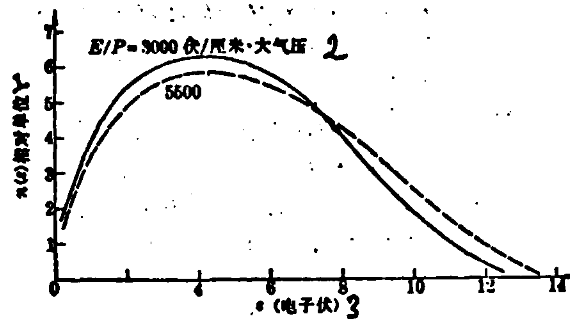

Figure 1. Relations of electron energy distribution function $n(\varepsilon)$ and of electron energy ε vs. the relative field strength E/P.
Key: 1--relative unit; 2--volt/cm·atm; 3-- electron energy

In the high energy region of the electron distribution function $n(\varepsilon)$, the variation in the field strength shows greater effect. The excitation ionization process of the ground state inert gas atoms is sensitive to the variation in E/P. It has been discerned [1,3] that in the discharge KrF^* laser, the effect pumping process is accomplished through the participation of Ar^* and Kr^* , therefore, suitably raising the relative field strength is advantageous to the formation of Ar^* and Kr^* . Figure 3 shows

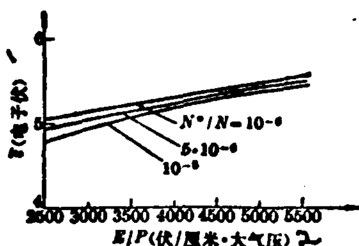

Figure 2. Relations of average electron energy $\bar{\varepsilon}$ and of meta-stable species fraction N^*/N to the relative field strength E/P.
Gas ratio: Ar:Kr:F_2=0.915:0.08:0.005;
Total pressure P=2 atm.
key: 1--electron volt;
2--volt/cm·atm

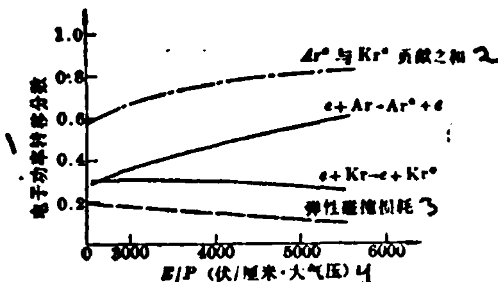

Figure 4. Relation of electron-atom elastic collision loss and of the meta-stable species Ar^* and Kr^* electron power ratio to the relative field strength E/P.
Ar:Kr:F_2=0.916:0.08:0.004;
P=2 atm; $N^*/N = 5\times10^{-6}$
Key: 1--electron power transfer ratio; 2--combined contribution of; 3--elastic collision loss; 4--volt/cm·atm

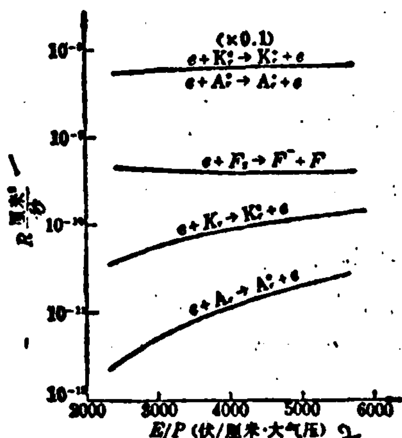

Figure 3. Relation between the relative field strength E/P and the coefficients of Ar and Kr meta-stable state production rate and meta-stable state ionization rate and the coefficient of dissociative adhesion rate of F_2.

Ar:Kr:F_2=0.916:0.08:0.004;
P=2 大气压; $N^*/N = 5\times10^{-6}$

Key: 1--cm^2/S; 2--(volt/cm·atm).

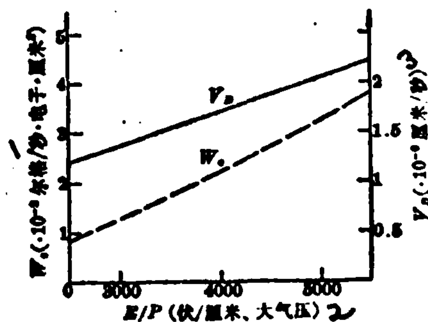

Figure 5. Relations between the relative field strength E/P with the drift velocity of the discharging electron (solid line) and the discharge power of each electron (dotted line).
Ar:Kr:F_2=0.916:0.08:0.004;
P=2 atm; $N^*/N = 5\times10^{-6}$
Key: 1--(erg/sec·electron·cm^3);
2--volt/cm·atm;
3--(cm/sec)

the variation of the rate constant of the principle production reaction for Ar^* and Kr^* with E/P. On the other hand, the ionization energies of Kr^* and Ar^* are low. They are respectively 4.1 and 4.2 eV. Hence, their reaction rate constants are very large.

3. Discharge power and the distribution of discharge energy

In Figure 4 are shown the principle processes for discharge power distribution in the discharge of Ar-Kr-F_2. It can be seen that the discharge energy fraction for the elastic collision loss decreases as E/P increases while the sum of the discharge energy fractions for Ar^* and Kr^* production has relatively more weight and also increases with increasing E/P. Within the ranges of N^*/N and n_e/N as discussed in this paper, roughly more than 60% of the discharge energy is used in producing Ar^* and Kr^* .

Figure 5 gives the variations of the discharge power W_e and the electron drift velocity V_D with E/P. Apparently, in this region of E/P, both increase linearly with E/P. For

$$n_e/N = 5\times 10^{-6},$$

at E/P = 3000 volt/cm·atm, the discharge power reaches 350 kw/cm^3.

4. Some effects of F_2

In Ar-Kr-F_2 discharge, F_2 plays a very important role although its content is only a few parts per thousand. When the electron energy distribution function is calculated in this paper, only the electron vibrational excitation process and the dissociation and adhesion effect of electrons on F_2 are taken into account while for lack of cross-sectional data, the various electronic transitions in the visible light region of F_2 are not considered. As pointed out in [16], these processes may have a definite cooling effect on the electronic energy. Computation indicates that the vibrational excitations do not have any remarkable effect on the electronic

energy distribution. These processes have cross-sections of the order of Å^2, but because of the low concentration of F_2 and of the fact that these transition quanta are as small as of the order of 0.1 eV, the overall effect is small. The fractional discharge energy for the dissipation through F_2 vibrational excitation is only about 1%. Figure 6 shows the relation between the variation of the average electron energy with the fractional density of F_2 under the computational conditions:

$$N^*/N = 10^{-6},\ Ar:Kr:F_2 = (0.92 - q_{F_2}):0.08:q_{F_2},$$

P=2 atm. It can be seen that in the range of F_2 content variation in this paper, the change in average electronic energy is very small.

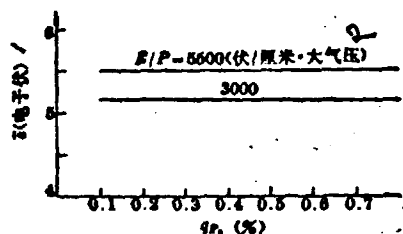

Figure 6. Relation between the average electron energy $\bar{\varepsilon}$ and the gm molecular ratio q_{F_2} of F_2. The parameters in the diagram is the relative field strength E/P; other conditions are $N^*/N = 10^{-6}$; $Ar:Kr:F_2 = (0.92-q_{F_2}):0.08:q_{F_2}$; P=2 atm; the electron F_2 electronic excitation and ionization processes have not been included.
Key: 1--(electron volt)
2--(volt/cm·atm)

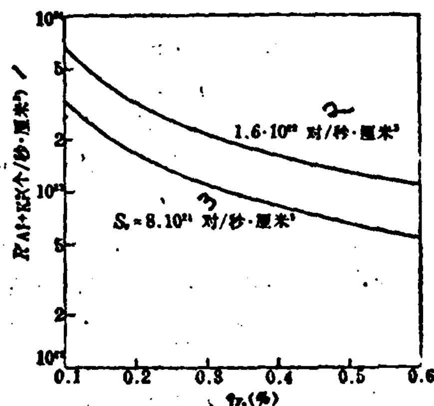

Figure 7. Relation of the rate constant of meta-stable species Ar^* and Kr^* production by electron collisions to the strength of external ionization source S_0 and to the fractional density of F_2.
$Ar:Kr:F_2 = (0.92-q_{F_2}):0.08:q_{F_2}$; P=2 atm; E/P=4000 volt/cm·atm, $N^*/N = 5\times10^{-6}$
Key: 1--(/sec·cm^3); 2--pairs/sec·cm^3; 3--pairs/sec·cm^3

The principle process for discharge electron dissipation in Ar-Kr-F_2 discharge is the electron F_2 dissociation-adhesion process.

It is obvious from Figure 3 that the rate constant β of this effect does not vary much with E/P. The computation also indicates that within the range of $N^*/N = (10^{-6} - 10^{-5})$ and $N_{F_2}/N = (0.1-0.8)\%$ $\beta \approx (4-5) \times 10^{-10}$ cm^3/sec.

Increasing the F_2 content is beneficial to the eventual formation of KrF^* by stable discharge and meta-stable reactions but in stable discharge the electron density $n_e = S_e/\beta N_{F_2}$, so that too high a value of F_2 content will greatly decrease the electron density. When the external ionization source strength S_e is maintained constant, the rate density $R'_{Ar^*+Kr^*} = (R_{Ar^*} N_{Ar} + R_{Kr^*} N_{Kr}) S_e/\beta N_{F_2}$ of meta-stable species production rapidly decreases with increasing N_{F_2}. Figure 7 shows the situation of this variation with the computational conditions. The diagram shows two S_e values corresponding respectively to the electron beam current density (300 KeV) of 5 and 10 amp/cm^2. Another problem that deserves attention is that F_2 has a strong quenching effect on KrF^* with a reaction constant as high as 7.8×10^{-10} cm^3/sec; at the same time F_2 has a sizable absorption at the wavelength of 249 milli-micron. According to the absorption cross-section provided by Steunenberg et al. [17], the value is about 1.3×10^{-20} cm^2. These factors severely limit the upper bound of F_2 gas density in KrF^* laser.

5. Effect of oxygen

The small amount of residual oxygen in the system has a large effect on the discharge characteristic of Ar-Kr-F_2. We have estimated this effect in this section. When solving the Boltzmann integro-differential equation, the following reaction processes involving the participation of oxygen are included: the dissociation adhesion process of electron-O_2 with a peak value of 6.7 eV [18,19]; the $^3P\text{-}^1D\ ^3P\text{-}^1S$ excitation process of electron on oxygen atom where the oxygen atom density is assumed to be $N_0 = 0.1 N_{O_2}$; the electron-O_2 ionization process; the electron-O_2 excitation

processes which include 3 excitation cross-sections obtained through computation based on the trapped electron data of Schultz and Dowell [22]. With the exception of the data for ionization cross-section, most of the other cross-sections are either the result of computation or obtained through indirect computation from experimental results. Thus, the calculation in this section is quite preliminary. Figure 8 shows the relation between the electron energy, the growth rate constant of standardized Ar^{*} and Kr^{*} as well as the discharge energy ratio for oxygen excitation and the fractional density $q_{O_2} = N_{O_2}/N$ of oxygen under the conditions indicated. Apparently, with the increase of oxygen density, both the average electron energy and the production rate constant of Ar^{*} and Kr^{*} decrease while the discharge energy for O_2 excitation increases. Because of the fact that the oxygen excitation cross-section processes are not completely mastered, the estimation of the above effects for O_2 is only approximate.

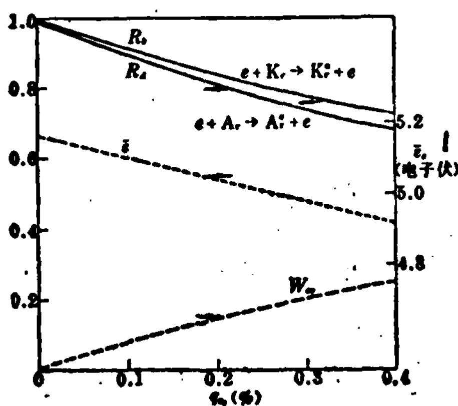

Figure 8. Relation of the average electron energy $\bar{\varepsilon}$ (dotted line), growth rate constant of standardized Ar^{*} and Kr^{*}, R (solid line) and the discharge energy ratio for oxygen excitation W_{O_2} to the fractional density of the oxygen molecule q_{O_2}

$N^{*}/N = 5\times10^{-4}$; $E/P = 3500$ volt/cm·atm; Ar:Kr:F$_2$ = 0.916:0.08:0.004; $P = 2$ atm;

Key: 1--electron volt

REFERENCES

[1] M. Rokni *et al.*; *IEEE J. Quant. Electr.*. 1978,

[2] Shao-Chi Lin *et al.*; *Appl. Phys. Lett.*, 1979, **34**, 505.

[3] W. L. Nighan; *IEEE. J. Quant. Electr.*. 1978, **QE-14**, 714.

[4] W. H. Long, Jr.; *Appl. Phys. Lett.*, 1977, **31**, 391.

[5] O. Judd; *J. Appl. Phys.*, 1976, **47**, 5297.

[6] L. S. Frost *et al.*; *Phys. Rev. A*, 1964, **136**, 1539.

[7] R. J. Hall; *J. Chem. Phys.*, 1978, **68**, 1803.

[8] J. H. Jacob *et al.*; *Appl. Phys. Lett.*, 1976, **29**, 467.

[9] M. Schaper *et al.*, *Beit. Plas. Phys.*, 1969, **9**, 45.

[10] J. Olmsted III *et al.*; *J. Chem. Phys.*, 1965, **42**, 2341.

[11] D. Rapp; *J. Chem. Phys.*, 1965, **43**, 1464.

[12] H. A. Hyman; *Phys. Rev. A*, 1978, **18**, 441.

[13] L. Vriens; *Phys. Lett.*. 1964, **8**, 260.

[14] S. D. Rockwood; *Phys. Rev. A*, 1973, **8**, 2348.

[15] K. Smith *et al.*; "Computer Modeling of Gas Lasers", Plenum Press, New York 1978.

[16] A. E. Greene *et al.*; *IEEE J. Quant. Electr.*, 1978, **QE-14**, 951.

[17] R. K. Steuneberg *et al.*; *J. Amer. Chem. Soc.*, 1956, **78**, 901.

[18] G. J. Schulz; *Phys. Rev.*, 1962, **128**, 178.

[19] J. D. Craggs *et al.*; *Proc. Roy. Soc.* (London); 1957, A-**240**, 473.

[20] R. J. W. Henry *et al.*; *Phys. Rev.*, 1969, **178**, 218.

[21] H. S. W. Massey; Electronic and Ionic Impact Phenomena; **2**, Oxford at the Clarendon Press; 1969, 1017.

[22] G. J. Schulz *et al.*; *Phys. Rev.*, 1962, **128**, 174.

Abstract: In this paper, some plasma properties of Ar–Kr–F_2 gas mixtures are calculated and discussed under the condition of steady discharge.

UV-PREIONIZED ArF AND KrF EXCIMER LASERS

Shangguan Cheng, Yuan Cailai, Ye Chao Dou Airong

(Shanghai Institute of Optics and Fine Mechanics)
Academia Sinica

ABSTRACT

Experimental investigations of UV-preionized ArF and KrF excimer lasers are reported. The output laser energies of 105 mJ for ArF and 185 mJ for KrF are obtained. Effects of various parameters on the laser characteristics are discussed.

UV-pre-ionized rare gas-Halogen excimer lasers are capable of outputting medium energy UV laser radiation [1~3]. Owing to their simplicity in construction and small sizes, they have the prospect of wide applications in such areas as pumping dye lasers, laser isotope separation, laser chemistry and nonlinear optics.

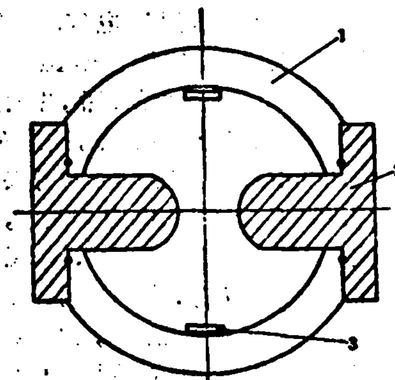

Figure 1. Laser cross-section
1. discharge chamber
2. electrodes. 3. pre-ionization spark gap

Our preliminary version of an excimer laser had a glass structure with wedge-shaped electrodes and employed NF_3 as donor for fluorine. In June, 1979, we obtained an ArF excimer laser of 1.5 mJ pulse energy [4]. Recently, we have improved on the design and substituted NF_3 with F_2, resulting in great improvement in its characteristics. A detailed account is reported below.

Received March 26, 1980

STRUCTURE OF THE LASER

Figure 1 shows the cross-sectional diagram of the laser. The discharge chamber is made of fibre glass tube (commonly known as epoxy tube) with an inner diameter of 8.4 cm and a length of 94 cm. The electrodes are Zhang's uniform field surface electrodes[4] made of brass plated with nickel. The width is 3 cm with an effectively flat region of 5 mm in the center and effective discharge length of 80 cm. The distance between the electrodes is 2.1 cm. The electrodes are connected to the discharge chamber with screws, sealed by fluorine-proof O rings. Under ordinary conditions, the vacuum achieved is of the order of 10^{-3} torr.

Pre-ionization is realized with the UV produced in the spark gap. The spark gap plates are placed on the upper and lower sides of the electrodes at a distance of 3.8 cm from the center of the principle discharge electrode. The base plate of the spark gap plate is a glass plate 90 cm long, 1.5 cm wide and 0.3 cm thick. The spark gaps are formed by gluing 29 nickel plates of width 27 mm, width 5 mm and thickness 0.1 mm on the glass plate with epoxy resin. The two structures of the spark gap plates as shown in Figure 2 both gave good results. In structure (a), long nickel strips of 5 mm width and 0.1 mm thickness are glued on the other side of the glass plate so as to form small condensers for each small nickel plate. No such structure in structure (b).

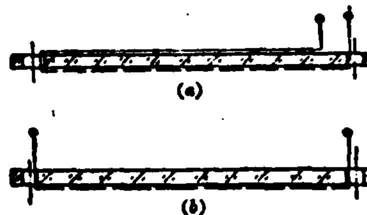

Figure 2. Diagram of pre-ionized spark gap plate.

Spherical gap switch is one of the key technology for this kind of laser device. We used a co-axial low inductive spherical gap we designed and constructed. It has a metal housing and can stand high gas pressure. The distance between the electrodes is

adjustable. Ordinarily, this distance is adjusted to be about 2mm.

The pre-ionizing capacitor is chosen to be non-inductive capacitor with a capacitance of 0.047 μf. The principle discharge capacitor is a flat plate condensor made from two sheets of copper foil of thickness 0.05 mm in parallel with a multilayer thin film of dacron of thickness 0.1 mm in the middle. The copper foil is 80 cm wide and 100 cm long . The dacron film has dimensions slightly larger than the copper foil in order to avoid electrical leakage at the edge between the upper and lower copper foil.

The optical cavity is formed by two aluminum-plated reflecting mirrors. The total reflective mirror has a radius of curvature $R=3\sim5$ meters and the partially reflective mirror has a radius of curvature $R=\infty$. The output is coupled with a rectangular opening. The distance between the two reflecting mirrors is 106 cm. Fluorine proof O rings are used to give a tight seal between the reflecting mirror and the laser chamber.

OPERATIONAL CONDITION AND LASER CHARACTERISTICS

The discharge circuit is chosen to be an LC reverse circuit. The principle is shown in Figure 3. The measured values for C_1 and C_2 are respectively 12 mμf and 25 mμf. SG_1 and SG_2 are respectively the pre-ionizing spark gap switch and the principle discharge spark gap switch. Before operating the apparatus, the spherical gap switch needs to be filled with nitrogen gas of suitable pressure (depending on the charging potential) before charging up the pre-ionizing capacitor C and the principle discharge capacitors C_1 and C_2. When the pre-ionizing spherical gap switch SG_1 is triggered first by a delay triggered output voltage pulse, the pre-ionized spark gap produces 60 sparks along the longitudinal direction of the apparatus to pre-ionize the gas mixture. After the first pulse with a delay of $1\sim5$ μsec, the delay trigger outputs a second pulse to trigger the principle discharge spherical gap switch SG_2, causing

SG_2 to conduct. C_1 then discharges through SG_2 so as to make the discharge uniform between the principle electrodes.

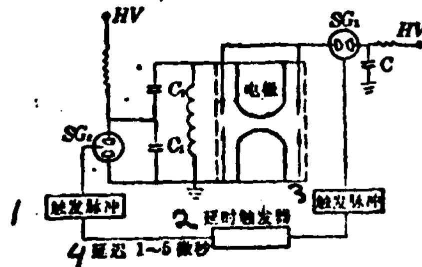

Figure 3. Diagram of LC reverse circuit

Key: 1--trigger pulse; 2--delay trigger; 3--trigger pulse; 4--1∿5 μsec

The output laser energy is closely related to the composition of the gas mixture. The result is shown in Figures 4 and 5. Figure 4 shows the results of the variation of the percentage content of the fixed gas total pressure Ar, the principle discharge voltage and pre-ionization condition, the output laser energy with the fluorine content. From the diagram, it can be seen that the optimum fluorine content is about 0.4%. Figure 5 shows the relation between the fixed gas total pressure, the percentage content of fluorine, the principal discharge voltage and pre-ionization condition and the output laser energy and the percentage content of Ar. From experiment, it can be seen that the optimum percentage argon content is about 20%.

For ArF, with a mixture of 0.4% F_2, 20% Ar and 79.6% He at a total pressure of 2.5 atmosphere, the maximum pulsed laser energy of 105 millijoules has been obtained. The laser wavelength is 1933Å.

For KrF, the maximum pulsed laser energy obtained is 185 millijoules at a laser wavelength of 2484Å. The gas mixture content is 0.3% F_2, 15% Kr and 84.7% He. Total pressure is 2.5 atm. The efficiency is 0.7%.

At 1933Å, when the output laser energy is greater than 50 mj, the aluminum film on the reflecting mirror shows damage. For wavelength 2484Å, the aluminum film shows damage only when the energy is

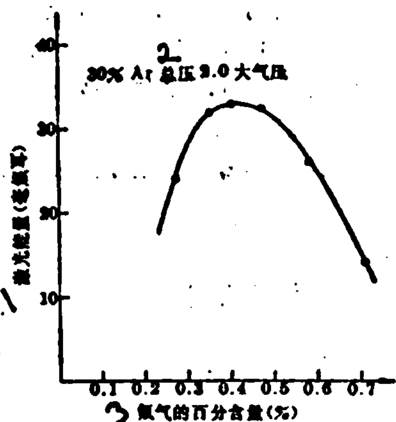

Figure 4. Relation between output laser energy and percentage fluorine content (principal discharge voltage 30 kilovolts)
Key: 1--laser energy millijoule 2--total Ar pressure 2.0 atm; 3--percentage content of fluorine (%)

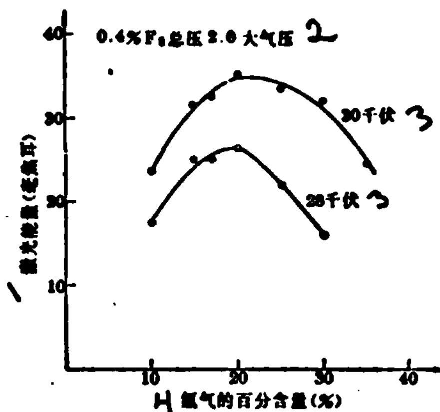

Figure 5. Relation between laser energy output and percentage content of argon.
Key: 1--laser energy (millijoules); 2--total F_2 pressure 2.0 atm; 3--kilovolts; 4--percentage content of argon

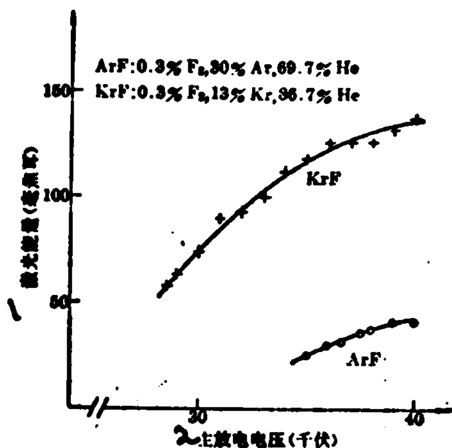

Figure 6. Relation between output laser energy and discharge voltage (total gas mixture pressure 2.3 atm)
Key: 1--laser energy (millijoules); 2--principal discharge voltage (kilovolt)

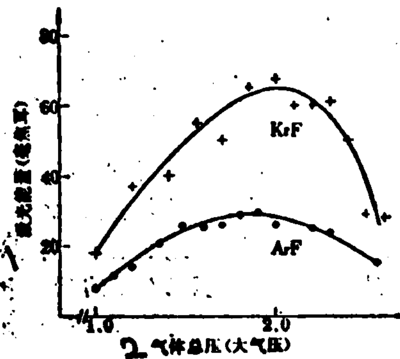

Figure 7. Relation between output laser energy and total gas pressure (principal discharge voltage fixed at 32 kilovolt)
Key: 1--laser energy (millijoules); 2--total gas pressure (atm)

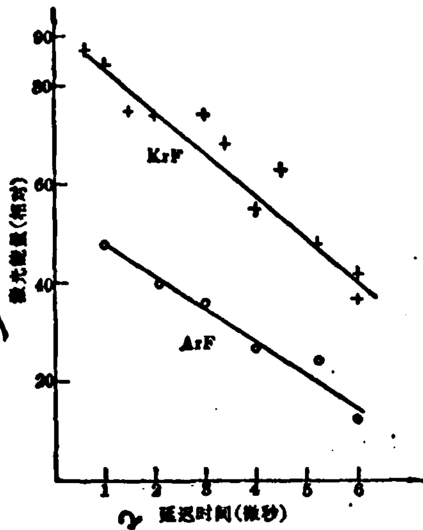

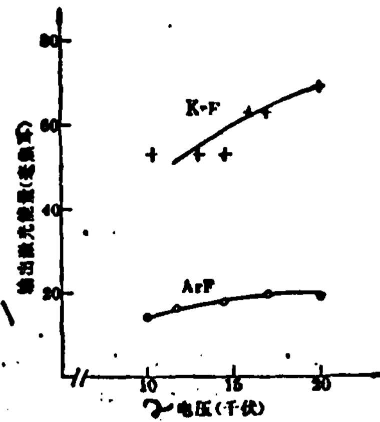

Figure 8. Relation between output laser energy and delay time
(ArF: principal discharge voltage 28 kv, total pressure 2.0 atm.
KrF: principal discharge voltage 30 kv, total pressure 2.5 atm)
Key: 1--laser energy (relative)
2--delay time (μsec)

Figure 9. Relation between output laser energy and pre-ionization voltage
(ArF: principal discharge voltage 28 kv, total pressure 2.0 atm.
KrF: principal discharge voltage 30 kv, total pressure 2.5 atm)
Key: 1--output laser energy (mJ)
2--voltage (kilovolt)

greater than 100 mJ [5]. We also observed that when the laser energy level is lower than the above mentioned values, repeated operations will cause damage on the aluminum film. The damaging of the aluminum film is more serious at the two ends of the light spot (2.1×0.5 cm^2).

The relation between the laser energy and the capacitor charging voltage has been measured in the experiment and the result is shown in Figure 6. We can see from the diagram that the laser energy does not increase linearly with the input electric energy, possibly because too high a voltage (or input energy) may change the electron energy distribution of the discharging gas, leading to the less efficient production of ArF and KrF pseudo-molecules as well as arcing.

Figure 7 shows the variational relationship between the output laser energy at fixed mixture composition and charging voltage with the total gas pressure. The maxima in the curves indicate that there is a certain charging voltage for a total gas pressure that gives a maximum laser energy output, i.e., the optimum $(V/P)_{charging}$ value. The $V/P_{charging}$ value measured in the diagram is ArF 11 volt/cm•torr KrF 10 volt/cm•torr.

The effect of pre-ionization on the output laser energy is large. Experiments indicate that the effect is best when the principle discharge occurs at the maximum pre-ionization discharge current, giving rise to a maximum in output laser energy. We have measured the variational relationship between the output laser energy and the delay time of the pre-ionization vs. the principal discharge. The result is shown in Figure 8. Ordinarily, the laser operates in the vicinity of a delay time of 1 μsec.

Figure 9 shows the relation between the laser energy and the pre-ionization capacitor charging voltage. It can be seen from the diagram that the laser energy increases with the pre-ionization voltage. This is because the increase in the pre-ionization voltage will fortify the spark strength and hence the pre-ionization effect. But too high a value of pre-ionization energy will lower the purity of the gas and shorten the laser lifetime. Thus, one should choose a moderate pre-ionization voltage in the experiment (∿20 kilovolt).

Abstract: UV-preionzed ArF and KrF excimer lasers are reported. Maximum pulse energies of 105 mJ in ArF and 185 mJ in KrF were extracted. In this paper we discuss the effect of various parameters on laser performances.

REFERENCES

[1] R. Burnham, N. Djeu; *Appl. Phys. Lett*; 1976, 29, 707.

[2] Robert C. Sze, Thomas R. Loree; *IEEE J. Quant. Electr.*, 1978, QE-14, 944.

[3] T. J. Mckee *et al.*; *IEEE, J. Quant. Electr.*, 1979, QE-15, 33.

[4] Shangguan Cheng, Yuan Cailai, Ye Chao, Dou Airong "UV pre-ionized ArF pseudo-molecular laser" unpublished.

[5] T. Y. Chang; *Rev. Scient. Instrum.*, 1973, 44, 405.

[6] J. N. Hoffman *et al.*; *Appl. Phys. Lett.*, 1976, 28, 538.

SCIENTIFIC NOTES

ND:YAG PULSED LASER OUTPUT AT 1.064, 1.073, 1.061 AND 1.052 μm SINGLET SPECTRAL LINES

Abstract: Single spectral lines at 1.064, 1.073, 1.061 and 1.052 μm were obtained respectively by inserting into the cavity the uncoated (or coated) solid etalons of 0.1 mm or both 0.1 mm and 0.14 mm thickness and appropriately controlling the gain of Nd:YAG laser and tilted angles of the etalons.

Various types of transitions [1] exist from $^4F_{3/2} \rightarrow {}^4I_{9/2}, {}^4I_{11/2}, {}^4I_{13/2}$ energy levels for Nd:YAG laser operating under room temperature. In the oscillational process, because of the competitive effect between the spectral lines, the 1.064 μm which has the largest excitation cross-section will be the first to oscillate. Thus under ordinary conditions, Nd:YAG has only the 1.064 μm oscillation output. To obtain the output at other spectral lines, we must suppress by some means the transition of the strong spectral line. The two commonly used techniques are the employment of a prism as a chromatic dispersion element [2] or the placement of an inclined etalon in the cavity. In this experiment, we have adopted the method of placing in the cavity etalons of various thickness with suitable coating and obtained the laser output at 1.064, 1.073, 1.061 and 1.052 μm singlet spectral lines in an attempt to solve the wavelength matching problem when Nd:YAG is used as an oscillator in high power laser systems and when Nd phosphate glass (central wavelength 1.054 μm) and Nd silicate glass (central wavelength 1.061 μm) are used as amplifiers.

We know from paper [5] that when an etalon is placed in a laser cavity, the shift Δλ in the central wavelength caused by its inclination angle θ is:

$$\Delta\lambda = \lambda_0\theta^2/2n^2 \text{ and } \Delta\nu = \nu_0\theta^2/2n^2 \quad (1)$$

where λ_o is the central wavelength.

The free spectrum range of the etalon is given by the following formula:

$$\Delta\nu = C/2nd \qquad (2)$$

The transmission characteristic of the etalon is

$$T \approx \left[1 + (2F/\pi)^2 \sin^2 \frac{2\pi nd\cos(\theta/n)}{\lambda}\right]^{-1} \qquad (3)$$

where $F = \pi R^{1/2}/(1-R)$, is the sharpness of the etalon, R the coating reflectivity and d the thickness of the etalon. For fixed wavelengths, the theoretical curve of the relationship between the inclination angle of the etalon and the transmissivity is shown in Figure 1.

After the etalon of suitable thickness is inserted in the cavity, the oscillation wavelength of the laser will make great changes. This is because the wavelength of the oscillation must not only possess larger transmissivity for the etalon, but also fit the condition of oscillation of the resonance cavity. The thickness of the etalon is first determined in accordance with the desired output wavelength in the experiment. Then the angle of inclination of the etalon is fine-tuned so that the desired wavelength lies at a maximum of the transmissivity in Figure 1 while also satisfying the oscillatory condition.

To control the strong spectral line oscillations at 1.064 and 1.061 μm more effectively, it is often necessary to insert two etalons of different thickness in the cavity. By tuning the two etalons to suitable inclination angles so that the 1.064 and 1.061 μm spectral lines are situated at the maximum dissipation state, it is then easier to make the weaker single spectral lines at 1.052 and 1.073 μm oscillate.

The laser has a semi-co-focal cavity formed by reflecting mirrors of radius of curvature 3 m. The Nd:YAG rod dimensions are $\phi 5 \times 40$ mm, with single lamp pumping. The rod is cooled by circulating water at constant temperature. Table 1 shows the results of output experiment of the spectral lines when the cavity output reflectivity is R=84%.

Table 1 indicates that when the output mirror reflectivity is high, one needs only to insert one uncoated etalon. The 1.061 μm oscillation output can be easily obtained as the strongest 1.064 μm transition has been suppressed. When the etalon is slightly coated and the reflectivity is 20-30%, two strong transitions (1.064 and 1.061 μm) are both suppressed. The single 1.073 and 1.052 μm output are obtained senarately. Figure 2 shows the curve relating the variation in the blackening of the two spectral lines at 1.064 μm and 1.061 μm with the inclination angle of the etalon. The range for the 1.061 μm line is wider, from 0°-5°36'.

Table 2 gives the output results of the spectral lines when the output cavity mirror's reflectivity is reduced to R=63%. Because of the reduction in reflectivity, it is necessary to increase the sharpness of the etalon or insert a second etalon in order to obtain the output from each single line. For output mirror at R=63% the mode locking oscillation condition is already satisfied [6].

In our experiment, we have also designed an output cavity mirror which has different reflectivities for different waves-lengths. Table 3 shows the experimental results for the spectral lines when this kind of cavity mirrors are coupled. Comparing Tables 3 and 2, we see that the tuned resonance range of, say, the 1.052 μm is larger than Table 2. This indicates that this cavity mirror is effective in suppressing the stronger lines and promoting the oscillation of the weaker lines.

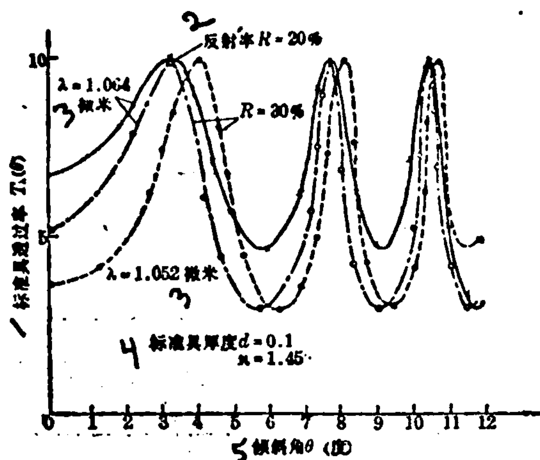

Figure 1. Theoretical curve of etalon inclination angle at fixed wavelength vs. transmissivity
Key: 1--etalon transmissivity; 2--reflectivity; 3--μm; 4--etalon thickness; 5--angle of inclination

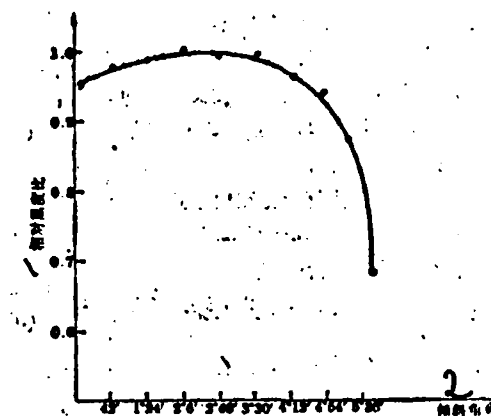

Figure 2. Variation of the blackening ratio of the two stronger spectral lines to the etalon inclination angle
Key: 1--relative blackening ratio; 2--angle of inclination

Finally, experiment also indicates that the surface parallelness and optical smoothness are important factors affecting the results. It is especially important during the coating process not to damage the etalon surface.

TABLE 1

wavelength (μm)		etalon parameter		tuned resonance range
1.061	singlet	d=0.1mm	uncoated	360-390 volt (150μf)
1.061	"	d=0.1 "	R=30%	780-900 volt (150μf)
1.073	"	d=0.1 "	R=20%	0- 4° (working under 1100 volt)
1.052	"	d=0.1 "	R=30%	750-780 volt (150μf)
1.073	"	d_1=0.1 " d_2=0.14"	uncoated R=30%	1°24'-3°30' (working under 900 volt)

TABLE 2

wavelength (μm)		etalon parameter		tuned resonance range
1.061	singlet	d=0.1 mm	R=20%	600-900 volt (150μf)
		d=0.1 "	R=40%	0-2°48' (working under 1200 volt)
1.073	"	d=0.1 "	R=30%	
		d=0.14 "	R≈30%	900-1050 volt (300μf)
1.052	"	d=0.1 "	R=20%	0-2°48' (1200 volt 150μf)
1.061	"			

TABLE 3

wavelength (μm)		etalon parameter		tuned resonance range	reflectivity of output cavity mirror	
1.061	singlet	d_1=0.1 mm d_2=0.14 "	R=30%	900-1500 volt	1.06 mm 1.05 " 1.073 "	R=65% R=70% R=50%
1.073	"	d=0.1 "	R=30%	720-900 volt (200μf)	\	
1.052	"	d_1=0.1 " d_2=0.14"	R=30%	960-1320 volt (200μf)		

References

[1] R. G. Singh, R. G. Smith *et al.*; *Phys. Rev. B*, 1974, 110, No. 6, 2566.

[2] R. G. Smith; *IEEE J. Quant. Electr.*, 1968, QE-4, 505.

[3] B. Jack; *IEEE J. Quant. Electr.*, 1977, QE-13,

[4] J. Marling; *IEEE J. Quant. Electr.*, 1978, QE-14, 56.

[5] Michael Hercher; *Appl. Opt.*, 1969, 18, 1103.

[6] Chen Shaohe, Chen Lanrong et al "Laser" 1980, 7, no. 2, 44
(Shanghai Institute of Optics and Fine Mechanics, Academia Sinica, Zhi Tingting, Chen Lanrong)

A NEW FEEDBACK CONTROLLED CURRENT STABILIZED POWER SUPPLY FOR GAS LASER

Abstract: A feedback-controlled current stabilized power supply for CO_2 wave-guide lasers is reported. Current is stabilized in the range of 2~4 mW, the unstability of the current is less than 1% with respect to 20% fluctuation of network voltage.

We adopted a current negative feedback control method by connecting the control transistor to the DC output end of an AC bridge rectifier and designed a current-stabilized power supply with output power of 2W for a CO_2 wave guide laser. The principal circuit and the voltage-current wave forms of the power supply are respectively shown in Figures 1 and 2.

Assume that the transformer SB is an ideal transformer with leakage inductance L_s = 0 and primary inductance L_1 = infinity; let the secondary load be a pure resistance R when converted to primary; let the current entering the base of the transistor BG be a constant i_{b0} . In the following we shall qualitatively analyze the control action of the transistor BG by using Figure 1(b) and

Figure 2. From Figure 1(b), it is known that the load current i_R is equal to the collector current i_c. Here we shall only analyze the instantaneous value of the power supply voltage e during the positive half cycle. The negative half cycle will be the same. In the period t_1-t_2, $0<e<E_1(E_1, E_2$ --some fixed value) $i_R=i_c=0$. during t_2-t_3, $E_1<e<E_2$, $i_R=i_c$ increases as e increases. During t_3-t_4, $e>E_2$, $i_R=i_c=\beta i_b$. During t_4-t_5, $E_1<e<E_2$, $i_R=i_c$ decreases as e decreases. In the period t_5-t_6, $e<E_1$, $i_R=i_c=0$ In reality, E_1, E_2 are all very small and the period t_3-t_4 is very long. Hence, the current flowing through the load i_R is a rectangular wave of frequency 50 cycles and width βi_b. Thus, if suitable current negative feedback can be applied to control the current i_b entering the base of the transistor, then current stabilized control may be achieved.

For a real transformer, the primary inductive reactance $Z=\omega L_1 \gg R$, therefore, we only need to consider the effect of leakage inductance L_s. Since the current in the leakage inductance L_s cannot jump, this will cause the leading and trailing edges of the rectangular current wave flowing through the load to deteriorate and the larger $\frac{L_s}{R}$ is, the worse will be the wave form. This not only increases the ripple in the secondary rectified output current, but will also affect the stability of the current. This point must be attended to when constructing the transformer.

The power supply designed according to the new current negative feedback control principle is used for CO_2 wave guide laser with the following parameters: onset voltage approximately 20 Kv, operating voltage 10-13 Kv, discharge current 2-4 mA. By using the new power supply, the current-stabilizing resistance in series with the laser tube may be reduced from the value of 2.8 MΩ for ordinary power supply to a value below 1.4 MΩ while the stability of the discharge current is greatly improved. The current instability corresponding to a ±20% variation of the network voltage is less than 1%.

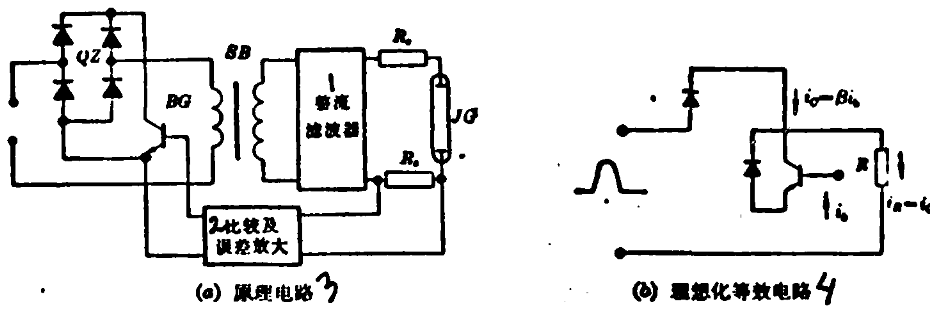

Figure 1. New feedback controlled current stabilizing power supply circuit.
Key: 1--rectifying filter; 2--comparative and error amplification; 3--(a) principle circuit; 4--(b)idealized equivalent circuit

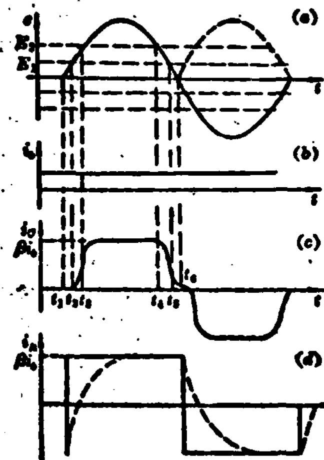

Figure 2. Wave forms for current and voltage at various points in the circuit

(Shanghai Institute of Optics and Fine Mechanics, Academia Sinica

Xie Guoliang, Shu Pujii, He Guopu
Received August 30, 1979)

DTIC